FEBS Letters 588 (2014) 1891–1898

FEBS Letters

journal homepage: www.FEBSLetters.org

Structural basis for recognition of the type VI spike protein VgrG3 by a cognate immunity protein

Jiulong Zhang [a,b,1], Heng Zhang [d,1], Zengqiang Gao [a], Haidai Hu [e], Cheng Dong [a,c,*], Yu-Hui Dong [a,*]

[a] Beijing Synchrotron Radiation Facility, Institute of High Energy Physics, Chinese Academy of Sciences, Beijing 100049, People's Republic of China
[b] School of Life Sciences, University of Science and Technology of China, 96 Jinzhai Road, Hefei, Anhui 230027, People's Republic of China
[c] State Key Laboratory of Medicinal Chemical Biology, Nankai University, Tianjin 300071, People's Republic of China
[d] State Key Laboratory of Protein and Plant Gene Research, and Biodynamic Optical Imaging Center (BIOPIC), School of Life Sciences, Peking University, No. 5 Yiheyuan Road, Beijing 100871, People's Republic of China
[e] Key Laboratory of Molecular Virology and Immunology, Institute Pasteur of Shanghai, Shanghai Institutes for Biological Sciences, Chinese Academy of Sciences, Shanghai, People's Republic of China

ARTICLE INFO

Article history:
Received 31 March 2014
Revised 9 April 2014
Accepted 9 April 2014
Available online 18 April 2014

Edited by Stuart Ferguson

Keywords:
The type VI secretion system
VgrG3–TsaB complex
Glycosyl hydrolase
T4-lysozyme-like fold

ABSTRACT

The bacterial type VI secretion system (T6SS) is used by donor cells to inject toxic effectors into receptor cells. The donor cells produce the corresponding immunity proteins to protect themselves against the effector proteins, thereby preventing their self-intoxication. Recently, the C-terminal domain of VgrG3 was identified as a T6SS effector. Information on the molecular mechanism of VgrG3 and its immunity protein TsaB has been lacking. Here, we determined the crystal structures of native TsaB and the VgrG3C–TsaB complex. VgrG3C adopts a canonical phage-T4-lysozyme-like fold. TsaB interacts with VgrG3C through molecular mimicry, and inserts into the VgrG3C pocket.

Structured summary of protein interactions:
VgrG3 and **TsaB** bind by x-ray crystallography (View interaction)
TsaB and **TsaB** bind by x-ray crystallography (View interaction)
VgrG3 and **TsaB** bind by cosedimentation in solution (View interaction)
TsaB and **TsaB** bind by cosedimentation in solution (1, 2)
TsaB binds to **VgrG3** by surface plasmon resonance (1, 2, 3, 4, 5, 6, 7)
VgrG3 and **TsaB** bind by molecular sieving (View interaction)
TsaB and **TsaB** bind by molecular sieving (View interaction)
VgrG3 and **TsaB** bind by x ray scattering (View interaction)

1. Introduction

The type VI secretion system (T6SS), a macromolecular nanomachine, is involved in the interaction with prokaryotic and eukaryotic cells [1]. The T6SS organelle is structurally and functionally analogous to contractile phage tails, including the spike, tube, sheath, and baseplate components [2–6]. Valine–glycine repeat protein G (VgrG), together with hemolysin coregulated protein (HCP), is secreted and required for the function of the T6SS machine, and represents the hallmark of T6SS [7]. Gram-negative bacteria expressing T6SS secrete and deliver toxic effector proteins into neighboring cells. The T6SS effectors destined for the periplasm degrade the cell wall and cell membrane of the receptor cells to kill the competitor cells, and the cognate immunity proteins expressed by the bacterium bind the effectors to prevent self-intoxication [8–13].

At present, several crystal structures of T6SS effector–immunity pairs have been determined [11,14–21], but these effectors are single-domain proteins and considered to transit via the HCP tube [22]. VgrG3 from *Vibrio cholera* consists of a bacteriophage-spike-like N-terminal domain (VgrG3N) acting as an important

Abbreviations: T6SS, the type VI secretion system; VgrG, valine–glycine repeat protein G; TsaB, the type VI secretion antitoxin B protein; AUC, analytical ultracentrifugation; SPR, surface plasmon resonance; SAXS, small-angle X-ray scattering

* Corresponding authors at: Beijing Synchrotron Radiation Facility, Institute of High Energy Physics, Chinese Academy of Sciences, Beijing 100049, People's Republic of China. Fax: +86 10 88233201.
E-mail addresses: dongcheng@ihep.ac.cn (C. Dong), dongyh@ihep.ac.cn (Y.-H. Dong).

[1] These authors contributed equally to this work.

http://dx.doi.org/10.1016/j.febslet.2014.04.016
0014-5793/

component of T6SS apparatus and a C-terminal domain (VgrG3C) which functions as a peptidoglycan-targeting glycoside hydrolase [10]. Recent studies have shown that VgrG3C plays a pivotal role in the fight against competitor cells as a unique T6SS effector and the type VI secretion antitoxin B protein (TsaB) inhibits VgrG3C to prevent self-killing [10,12]. However, the structure of the VgrG-related effector has not yet been reported, which restricts our understanding of the VgrG and T6SS mechanisms.

Here, we first report the crystal structure of the VgrG-related T6SS effector (VgrG3C). VgrG3C displays a phage-T4-lysozyme-type fold. Compared with its structural homologs, VgrG3C displays several unique features, which are associated with its substrate specificity. The catalytic residues of VgrG3C are identified in this study. The immunity protein TsaB interacts extensively with VgrG3C, destroying the enzymatic activity of VgrG3C. Unlike other T6SS immunity proteins, TsaB tends to form oligomer. Importantly, the oligomerization of TsaB is involved in the inhibition of VgrG3C. Structural clarification of the VgrG3C–TsaB complex has revealed the inhibition mechanism. Our work also extends our understanding of the role of T6SS in interspecies competition.

2. Materials and methods

2.1. Protein expression and purification

The DNA encoding the C-terminal domain of VgrG3 (amino acids 731–1009) was amplified by PCR from the genomic DNA of *Vibrio cholerae*, and ligated into a BamHI/XhoI-digested pET21a(+) (Novagen) vector. The plasmid of VgrG3C was transformed into Escherichia coli BL21 (DE3) competent cells for induced expression with 0.2 mM isopropyl-β-D-1-thiogalactopyranoside (IPTG) at 289 K overnight. The cells were harvested by centrifugation and resuspended in buffer containing 20 mM Tris pH 8.0, 150 mM NaCl, 2 mM β-Mercaptoethanol, 0.1 mM Phenylmethylsulfonyl Fluoride (PMSF), 10 μg/ml DNaseI and 1 mM $MgCl_2$. Cells were lysed by French press and cell debris was removed by centrifugation at 30000×g for 50 min. The supernatant was purified by nickel affinity chromatography. The expression and purification of TsaB (amino acids 27–122) were performed as described previously [23]. The elution of VgrG3C was concentrated and directly applied to gel filtration (Superdex™ 200 10/300 GL, GE Healthcare). The fractions of VgrG3C and TsaB were mixed, and then applied to gel filtration chromatography. The buffer for gel filtration contained 20 mM Tris pH 8.0, 150 mM NaCl and 1 mM DTT. Pooled the complex peak and concentrated to ~12 mg/ml prior to the crystallization trial.

2.2. Crystallization and data collection

VgrG3C-TsaB complex was crystallized at 277 K using sitting-drop vapour-diffusion technique. The crystals of the native complex were grown by mixing 1 μl of protein solution with 1 μl reservoir solution consisting of 0.1 mM HEPES pH 7.6 and 16% (*w*/*v*) PEG3350. The crystals were transferred into cryoprotectant solution (reservoir solution supplemented with ethylene glycol up to 10% (*v*/*v*). The selenomethionine (Se-Met) complex was purified and crystallized essentially in the same conditions as native complex. The crystallization of TsaB was performed as described previously [23]. The X-ray diffraction data were collected at beamline 3W1A of Beijing Synchrotron Radiation Facility (BSRF), China. All datasets were processed with HKL2000 [24].

2.3. Structure determination and refinement

The structure of complex was solved by single-wavelength anomalous diffraction (SAD) method, the initial phases were determined using AutoSol in the PHENIX [25–27] software package, and density modification and automatic model building were subsequently performed using AutoBuild routine in PHENIX [28]. Further model was manually built by the program COOT [29]. All the structure refinements were performed by phenix.refine [30] of the PHENIX package. The final model quality was checked with MolProbity [31] from the GUI of PHENIX. The structure of TsaB was determined by molecular replacement method with AutoMR [26] from the GUI of PHENIX using TsaB of Se-Met complex structure as a search model. Detailed data collection and refinement are presented in Table 1. All the structure figures were generated by PyMol [32].

2.4. Analytical ultracentrifugation (AUC)

For the AUC experiment, proteins were purified as described above. AUC was performed using Beckman XL-I analytical ultracentrifuge equipped with an An60Ti rotor speed of 60000 rpm at 293 K. All the data were processed by SEDFIT program [33].

2.5. Surface plasmon resonance (SPR)

Binding affinity of effector and immunity was measured by the technique of surface plasmon resonance (SPR) using a BIAcore T100 (GE Healthcare) with single-cycle kinetics method. TsaB (1 μg/ml in 10 mM sodium acetate, pH 4.5) was immobilized on a CM5 sensor chip (GE Healthcare) up to level of 100RU. VgrG3C and its mutants were injected over the sensor chip surface in running buffer (10 mM HEPES pH 8.0, 150 mM NaCl and 0.005 % (*v*/*v*) Tween-20) for 60 s at a flow rate of 30 μl/min. The dissociation occurred in running buffer for 720 s at the same flow rate and the sensor chip was regenerated with 10 mM NaOH for 20 s. Data were analyzed by 1:1 binding model using BIAcore T100 Evaluation software (GE Healthcare).

2.6. Small-angle X-ray scattering (SAXS)

SAXS experiments were performed at beamline 1W2A station in BSRF using a MARCCD165 detector. The proteins were diluted to 2–4 mg/ml in SAXS buffer (20 mM Tris pH8.0, 150 mM NaCl and 0.2 mM DTT). The experimental one-dimensional data were generated by PRIMUS [34] software from ATSAS suite. Subsequently, the

Table 1
Data collection and refinement statistics.

	SeMet-VgrG3C-TsaB	Native-TsaB
Data collection		
Space group	*C2*	$P2_12_12_1$
Resolution (Å)	50.00–2.40(2.49–2.40)*	50.00–2.79(2.85–2.79)
R_{sym} or R_{merge}	7.3(54.8)	7.7(40.1)
$I/\sigma I$	27.6(2.9)	25.0(3.0)
Completeness (%)	99.7(98.1)	98.4(99.4)
Redundancy	7.5(6.1)	5.9(5.7)
Refinement		
Resolution (Å)	38.16–2.40	44.12–2.79
No. reflections	19076	15700
R_{work}/R_{free}	21.09/25.60	22.26/27.96
No. atoms		
Protein	2343	4361
Water	107	38
B-factors		
Protein	49.66	56.77
Water	48.34	34.58
R.m.s. deviations		
Bond lengths (Å)	0.009	0.0134
Bond angles (°)	1.048	1.545

* Values in parentheses are for highest-resolution shell.

GNOM [35] was performed to evaluate the particle distance distribution function $p(r)$. The theoretical curves derived from CRYSOL [36] were fitted to the 2-fold complex crystal structure. The *ab inito* shape was reconstructed by a chain-like ensemble of dummy residues using GASBOR [37] program. The final model was averaged by DAMAVER [38].

2.7. Cell viability assay

VgrG3 (amino acids 731–1009) and TsaB (amino acids 27–122) were expressed in the periplasm using pET-22b(+) (Novagen) and pET-26b(+) (Novagen) vector with a signal peptide, respectively. The bacteria were incubated in LB medium at 310 K overnight, and serial 10-fold dilutions were plated onto LB plates carrying 0.03 mM IPTG for the induced expression. The variants were performed with the same protocol.

3. Results

3.1. Structure of the VgrG3C–TsaB heterotetramer complex

The structure of the C-terminal domain of VgrG3 (amino acids 731–1009) complexed with TsaB (amino acids 27–122) was determined at 2.4 Å resolution. The asymmetric unit contains a VgrG3C–TsaB heterodimer. However, the molecular mass of the complex, measured by filtration chromatography and analytical ultracentrifugation (AUC), indicates that the complex behaves as a heterotetramer in solution (Figs. 1A and 2). The complex was further investigated with small-angle X-ray scattering (SAXS). The experimental SAXS data was fitted well to the theoretical curve derived from the crystallographic heterotetramer (Fig. 1B). Additionally, the models generated independently according to crystal packing and SAXS were also consistent, confirming the heterotetramer structure of VgrG3C–TsaB in solution. The heterotetramer structure can be created by symmetry-related neighboring molecules (Fig. 1C).

3.2. Potential active site in VgrG3C

The overall structure of VgrG3C demonstrates a T4-lysozyme-like architecture (Fig. 3A). Gel-filtration experiments combined with AUC confirmed the monomeric nature of VgrG3C (Figs. 3B and 2). The structure consists of eight α-helices and two 3_{10} helices, which pack against three-stranded antiparallel β-sheets. The VgrG3C protein is characterized by two lobes (the C-lobe and the N-lobe) linked by a backbone helix (α4 helix). The conserved residues are mainly clustered around the cleft formed by the two lobes (Fig. 3A, right). A DALI [39] search for structural homologs revealed several candidates, including the chitosanase from *Streptomyces* sp. N174 (N174 chitosanase), the chitosanase from *Bacillus circulans* MH-K1 (MH-K1 chitosanase), and the pesticin from *Yersinia pestis*.

The electrostatic profile of VgrG3C is quite different from those of its structural homologs, suggesting that the substrates of these proteins diverge. The active clefts of the chitosanases are highly acidic, providing suitable sites for the chitosanases to bind the polycationic chitosans [40–44] (Fig. 4B–D). However, both basic and acidic patches are distributed around the cleft of VgrG3C (Fig. 4A).

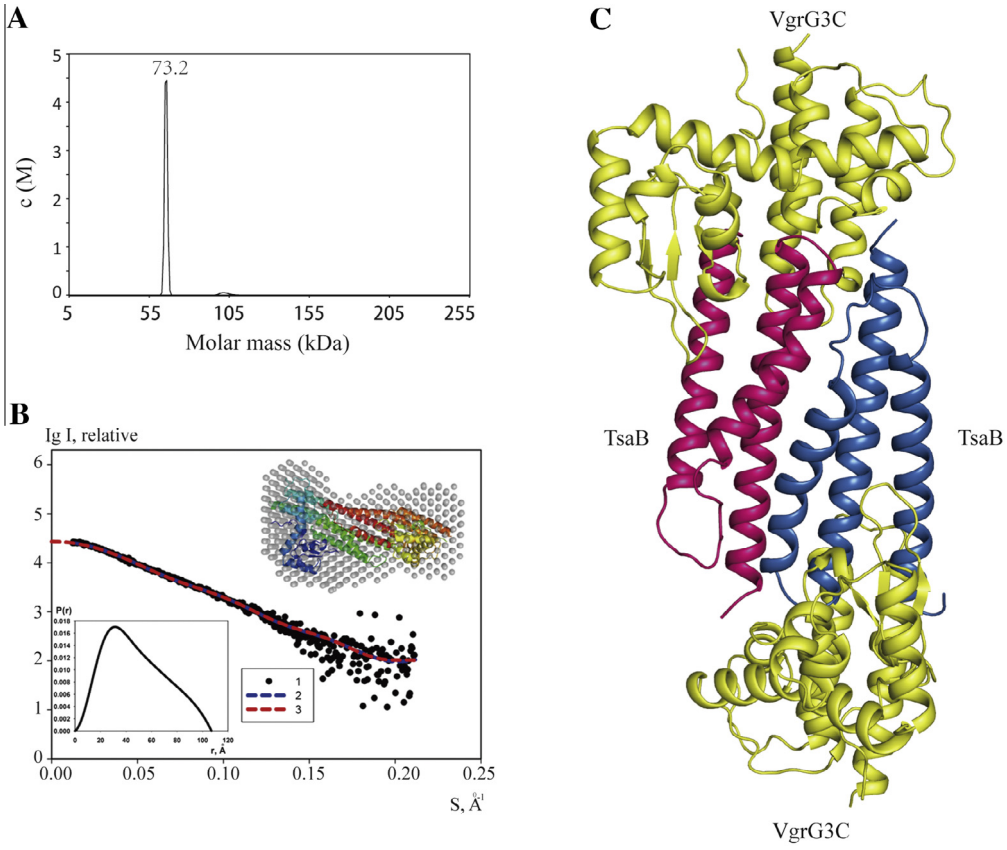

Fig. 1. Heterotetrameric state in solution and crystal structure of VgrG3C–TsaB complex. (A) Analytical ultracentrifugation analysis (AUC) of the VgrG3C–TsaB complex. The results show a main peak at 73.2 kDa, corresponding to the 84-kDa heterotetrameric complex. (B) Solution conformation and assembly of the VgrG3C–TsaB complex. Curve1, experimental scattering curve. Curve2, theoretical scattering curve from the heterotetramer curve. Curve3, the transformed $p(r)$ curve by extrapolated to zero scattering angle. The experimental SAXS curve is consistent with the heterotetramer curve. Right above: superimposition of the SAXS model and the crystallographic structure of the VgrG3C–TsaB heterotetramer. (C) Overall structure of the VgrG3C–TsaB heterotetramer. The heterotetrameric structure is generated by crystal packing, with VgrG3C in yellow and TsaB in pink and blue.

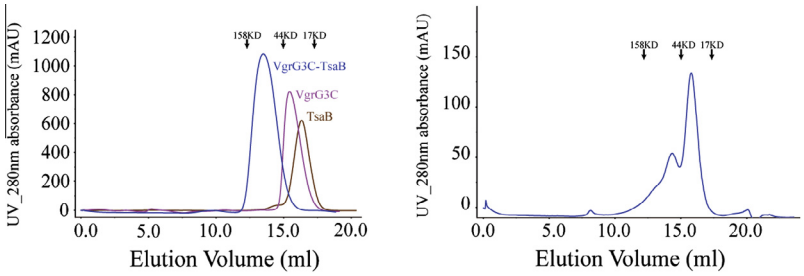

Fig. 2. Solution behavior of VgrG3C, TsaB, and the VgrG3C–TsaB complex. Left: Gel-filtration chromatograms of VgrG3C, dimeric TsaB, and VgrG3C–TsaB. Right: Gel-filtration chromatograms of oligomeric TsaB.

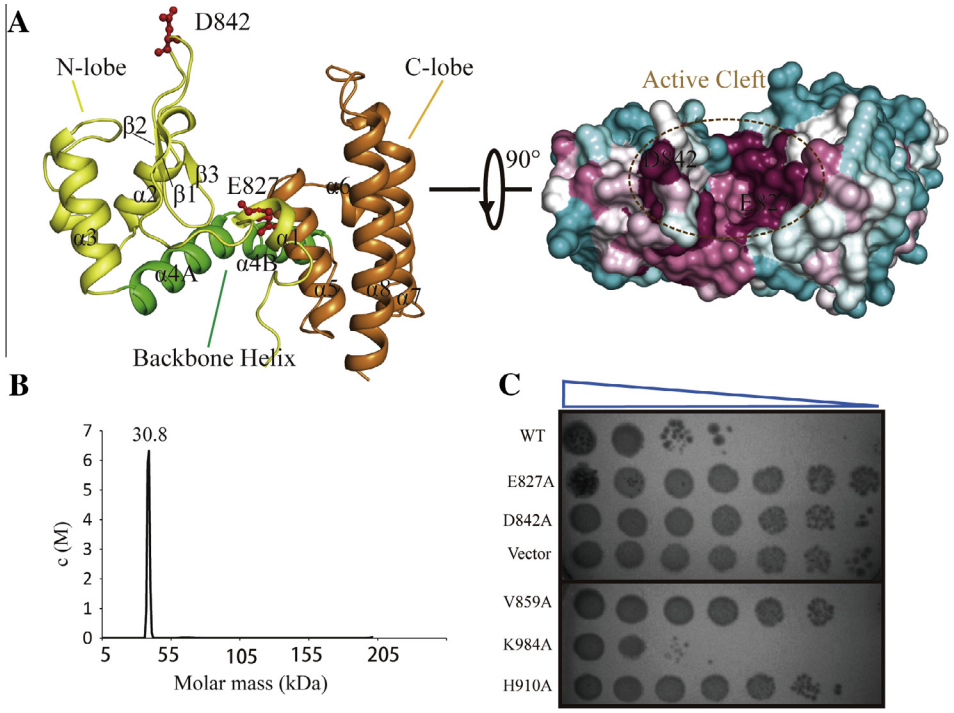

Fig. 3. VgrG3C structure and the potential active site. (A) Left: VgrG3C is divided into the N-lobe (yellow), C-lobe (orange), and the backbone helix (green). The catalytic residues are shown in stick representations. Right: Conserved residues are mapped onto the VgrG3C surface. Highly conserved residues are shown in maroon and the most variable residues in cyan. The catalytic residues are labeled. (B) Schematic diagram of AUC. VgrG3C behaves as a monomer in solution. (C) Identification of the active site of VgrG3C with a cell growth assay. The strains containing the periplasmic expression vector were serially diluted and plated onto IPTG agar plates. The VgrG3C wild type and mutants were present in the periplasm. The cells were killed if the VgrG3C variants retained activity.

Bioinformatic and structural analysis revealed that two invariant amino acids, Glu827 and Asp842, constitute the active dyad residues of VgrG3C. The variants E827A and D842A failed to suppress *Escheichia coli* growth, suggesting that the catalytic dyad is essential for the activity of VgrG3C (Fig. 3C). The catalytic mechanisms of glycosyl hydrolases are characterized by the distance between the catalytic residues [40]. The distance between Glu827 and Asp842 is above 10 Å, indicating the inverting mechanism. The proposed catalytic details can be inferred from the structural homologs [40–44]. Glu827, which is positioned at helix α1, contributes to the protonation process of sugar. Asp842 is believed to act as a general base, activating a water molecule to attack at the sugar's carbon.

In addition, three potential active-site mutations based on structural comparison (V859A, H910A and K984A) also have been tested. The result shows that V859A substitution abolished the activity of VgrG3C, the H910A variant located between helices α4A and α4B of VgrG3C was found to disrupt its enzymatic activity. The H910A variant may change the backbone helix orientation, which influences the shape and volume of the active cleft. But the mutation of Lys984 had no observable effect on the activity of VgrG3C (Fig. 3C).

3.3. TsaB tends to form homo-oligomers

Although dimeric TsaB accounts for most of the total protein, higher oligomeric assemblies also occur in solution. The AUC and gel-filtration results are fully consistent (Figs. 5A and 2). The structure of native TsaB was determined at a resolution of 2.8 Å. There are six molecules in an asymmetric unit, which consists of three TsaB dimers (Fig. 5B). TsaB folds into a three-helix bundle. The six individual molecules are generally well superimposed. Apo-TsaB dimer is nearly identical to the TsaB dimer in a complex (Fig. 5C). It is noteworthy that TsaB molecules also generate distinct interfaces in the native structure (such as the B–C interface and D–E interface), suggesting that these interaction modes may be involved in the formation of higher oligomers (Fig. 5B).

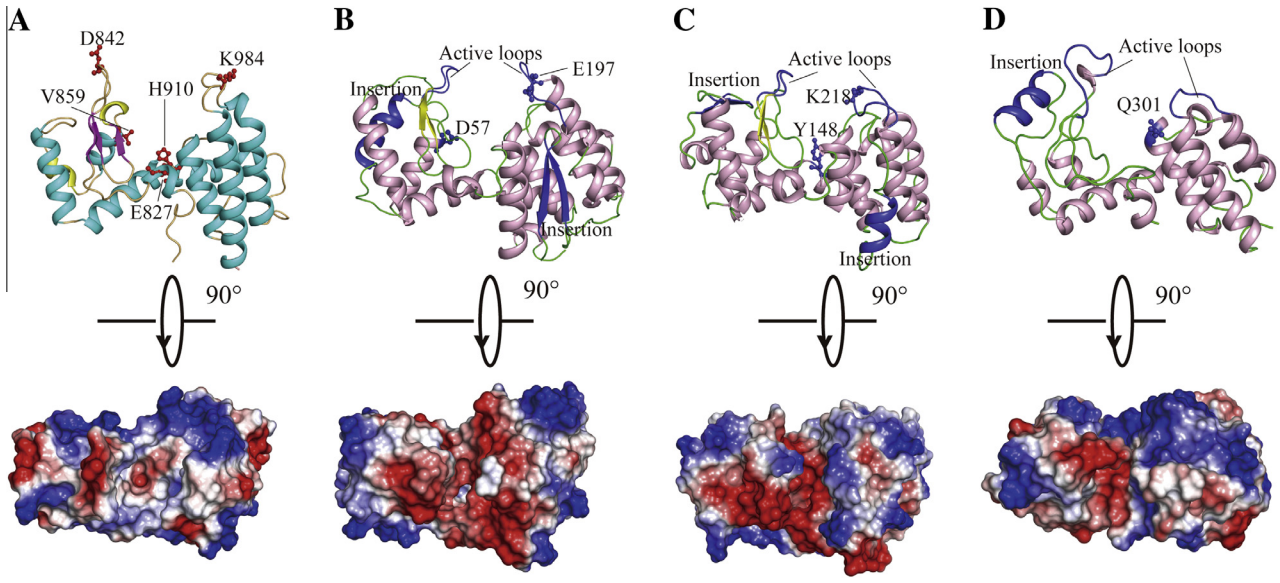

Fig. 4. Structural comparison with VgrG3C homologs. (A) Above: Cartoon representation, with secondary structure assignments, of VgrG3C. Helices, strands, and 3_{10} helices are shown in cyan, magenta, and yellow, respectively. The potential active sites are displayed in stick representations. Below: VgrG3C is represented by its electrostatic surface potential. The electrostatic surface on both sides is dominated by the cationic potential, whereas the central cleft is rich in negatively charged residues. (B–D) Above: Ribbon diagrams of N174 chitosanase (PDB: 1CHK) (B), MH-K1 chitosanase (PDB: 1QGI) (C), and pesticin (PDB: 4ARQ) (D). The insertions are colored blue. The active loops and active residues are labeled. Below: The structures are shown in electrostatic surface representations. In these proteins, the cleft is generally acidic.

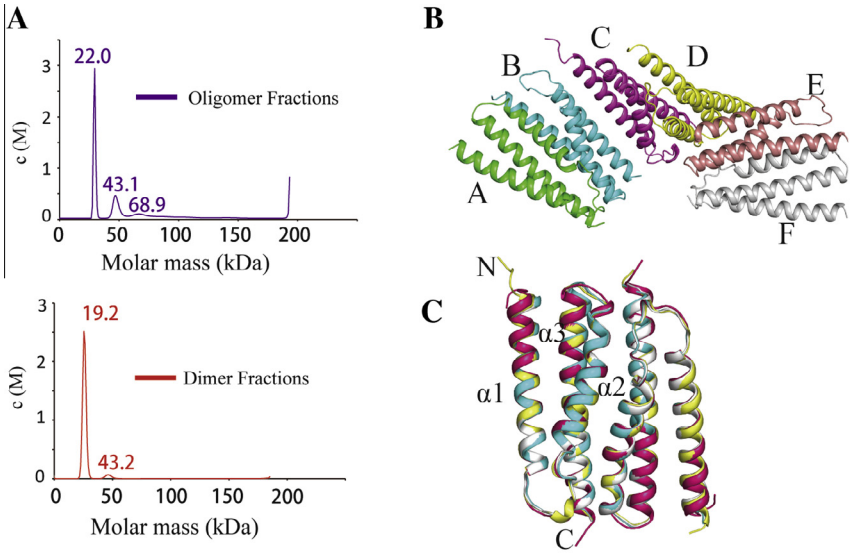

Fig. 5. Crystal structure of TsaB. (A) AUC profiles of oligomeric TsaB fractions (above) and dimeric TsaB fractions (below). The peaks indicate the different oligomeric states of TsaB. (B) Crystal structure of TsaB. Each monomer is labeled. (C) Superimposition of three native dimers with the dimer in the VgrG3C–TsaB complex. Each dimer is highlighted in a different color.

Fractions eluted from gel-filtration containing the TsaB dimer were collected, and then analyzed using AUC (Fig. 5A, below). Higher oligomeric TsaB was found, indicating that TsaB has a tendency to form oligomers.

3.4. Interaction of VgrG3C with TsaB

TsaB inserts deeply into the VgrG3C cleft, giving rise to an interaction interface of ~1160 Å^2 (Fig. 6A). Tyr826, adjacent to the catalytic residue Glu827 of VgrG3C, donates a hydrogen bond to His35 of TsaB. Notably, the catalytic residue Asp842 of VgrG3C mediates a number of hydrogen bonds with residues Glu50, Arg54 and Tyr71 of TsaB. Hydrogen bonding also occurs between Asn840 of VgrG3C and Asn44 of TsaB (Fig. 6B). Similarly, three conserved residues (Val941, Gln942, and Arg996) located in the C-lobe of VgrG3C are anchored by their interactions with Gln91 and Arg92 of TsaB. Hydrogen bonds between Asp992 of VgrG3C and Thr31 of TsaB and between the backbone oxygen in Leu982 of VgrG3C and the side-chain nitrogen in Arg92 of TsaB further stabilize the complex (Fig. 6C).

To characterize the VgrG3C–TsaB interaction in further detail, we performed affinity and kinetic analyses using SPR (Table 2). Two residues of VgrG3C (Ser837 and Gln852) that are involved in its water-mediated interactions with TsaB were also selected for study. VgrG3C binds to TsaB with high affinity (Kd = 0.98 nM). The Y826A, D842A, V941A, Q942A, L982A, and R996A variants

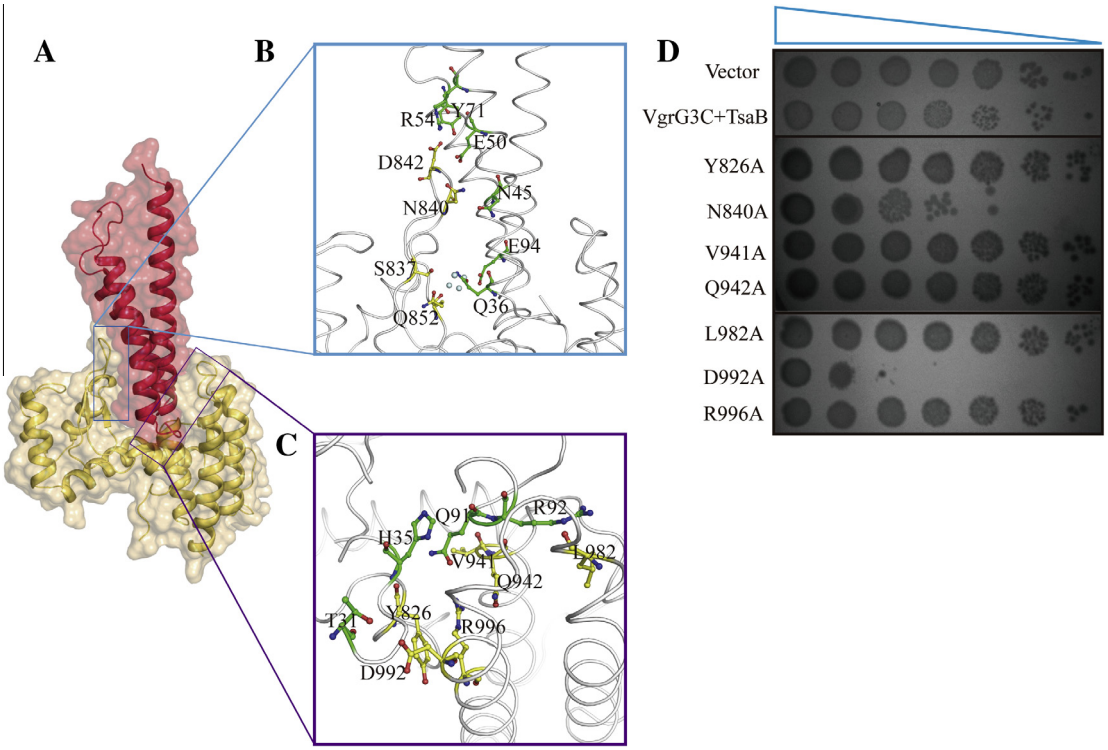

Fig. 6. Interaction of VgrG3C with TsaB and the mode of inhibition. (A) Surface representations of the heterodimeric VgrG3C–TsaB complex. The heterodimer is identical to the other one across a crystallographic axis of twofold symmetry. The heterodimer is only described for clarification. The coloring scheme is as described in Fig. 1C. (B–C) A close-up view of the VgrG3C–TsaB complex interface. The residues and water molecules involved in the interaction are shown as sticks and spheres, respectively. (D) Above panel, growth of *E. coli* cells in the presence of TsaB and VgrG3C. The cells were rescued by the expression of TsaB. Below panel, growth of *E. coli* cells in the presence of VgrG3C mutations. The cells were prepared as serial 10-fold dilutions.

Table 2
Binding affinity parameters for wild-type and mutant VgrG3C binding to TsaB.

VgrG3C mutants	Binding affinity Kd (M)
WT	9.78E-10
Y826A	3.33E-09
S837A	7.71E-10
N840A	7.96E-10
D842A	1.88E-09
Q852A	8.18E-10
V941A	3.23E-09
Q942A	4.94E-09
L982A	2.11E-09
D992A	5.54E-10
R996A	1.79E-09

were observed to cripple the interactions with TsaB. Notably, Tyr826 and Asp842 are closely associated with the activity of VgrG3C. However, substitutions S837A, N840A, Q852A and D992A did not appear to affect VgrG3C binding, indicating that the water-bridge contacts mainly complement the direct interactions. Intriguingly, the majority of critical residues linked to the affinity cluster in the C-lobe, suggesting that the C-lobe is responsible for the binding of VgrG3C to TsaB.

3.5. Mechanism of VgrG3C inhibition by TsaB

The active pocket of VgrG3C is occluded by TsaB, thereby inhibiting the activity of VgrG3C (Fig. 6A). Interestingly, several active-site residues in its structural homologs are equivalent to the TsaB-binding residues in VgrG3C. Therefore, we proposed that TsaB partly mimics the substrate of VgrG3C to trap its active site. We used point mutations and cell assays to confirm this proposition. As anticipated, most mutations of the TsaB-binding residues rendered VgrG3C inactive (Fig. 6D). In contrast, the substitution of Asp840 and Asp992 did not appear to affect the activity of VgrG3C. Most notably, the results are consistent with the VgrG3C–TsaB interaction analysis: only the D840A and D992A variants had little or no effect on TsaB-binding (Table 2). Together, these results suggest that TsaB inhibits VgrG3C through the molecular mimicry of its substrate.

The two loops of β1–β2 and α7–α8 in the VgrG3C–TsaB complex structure are fixed, however, a fair degree of flexibility in the corresponding loops is required for structural homologs activity [40–44]. Given the interactions between TsaB and these loops, we infer that these loops undergo structural rearrangement when native VgrG3C is incorporated into the VgrG3C–TsaB complex. These active loops in VgrG3C are considered to be mobile in the absence of immunity proteins.

4. Discussion

Bacteria have evolved various mechanisms to compete against each other [45]. One such mechanism involves the injection of effector proteins into the receptor cells via T6SS [8–13]. The C-terminal extension of VgrG3 acts as a lysozyme-like effector. TsaB, the antagonistic immunity protein, is used to prevent the self-destruction of the donor cell. In this study, we have performed structural and biochemical analyses of VgrG3C and TsaB. Overall, VgrG3C displays a canonical T4-lysozyme-like fold (Fig. 3A). We identified the catalytic dyad using cell assay and structural analysis. A long flexible linker (amino acids 731–815) connects VgrG3C to VgrG3N. The linker could not be mapped because of its flexibility, suggesting the dynamic nature of VgrG3C [5]. In addition, VgrG3C is also thought to dissociate from VgrG3N [10], and could be randomly distributed

in the periplasm. As a result, VgrG3C is more accessible to the substrate. This also explains why the bacterial cell wall tends to be very susceptible to VgrG3 [10,12]. However, there must be effective strategies to protect the donor and sister cells. The presence of different oligomeric forms of TsaB may be related to the dynamic nature of VgrG3C. In other words, dynamic TsaB proteins can effectively bind to the VgrG3C protein in multiple directions. The structures identified here, together with the experimental investigations undertaken, provide insight into how TsaB inactivates VgrG3C. In our proposed model, TsaB acts as a molecular mimic of the VgrG3C substrate, inducing an open conformation of the active loops of VgrG3C. The active loops move outward, removing the steric constraint. As a result, the active cleft is blocked by TsaB and the activity of VgrG3C is abolished. To our knowledge, this unique mode of inhibition is described for the first time here.

In summary, combined with a structural analysis, these biochemical data offer a framework with which to understand the mechanism and functions of VgrG3. The emergence of drug-resistant bacteria has become a critical problem and the major limitation of bacteriophage therapy is its inability to kill Gram-negative bacteria [44]. In this context, VgrG3C can potentially be used in the fight against Gram-negative bacteria.

Accession codes

The atomic coordinates and structure factor for SeMet-VgrG3C-TsaB complex and Native-TsaB have been deposited in the Protein Data Bank with accession codes 4NSO and 4NSR, respectively.

Acknowledgments

This work was supported by a Grant from the National Basic Research Program of China (2012CB917203) and the National Natural Science Foundation of China (10979005).We would like to thank the staff of the Beijing Synchrotron Radiation Facility (BSRF) for help with the diffraction data collection, Wenjia Wang for the SAXS discussion. Yuanyuan Chen and Bingxue Zhou (The Institute of Biophysics, Chinese Academy of Sciences) for the SPR experiment and Xiaoxia Yu (The Institute of Biophysics, Chinese Academy of Sciences) for the AUC experiment. We thank Dr. Stefan Pukatzki (University of Alberta, Canada) for kindly providing the VgrG3 plasmid.

References

[1] Hayes, C.S., Aoki, S.K. and Low, D.A. (2010) Bacterial contact-dependent delivery systems. Annu. Rev. Genet. 44, 71–90.
[2] Leiman, P.G., Basler, M., Ramagopal, U.A., Bonanno, J.B., Sauder, J.M., Pukatzki, S., Burley, S.K., Almo, S.C. and Mekalanos, J.J. (2009) Type VI secretion apparatus and phage tail-associated protein complexes share a common evolutionary origin. Proc. Natl. Acad. Sci. USA 106, 4154–4159.
[3] Pell, L.G., Kanelis, V., Donaldson, L.W., Howell, P.L. and Davidson, A.R. (2009) The phage lambda major tail protein structure reveals a common evolution for long-tailed phages and the type VI bacterial secretion system. Proc. Natl. Acad. Sci. USA 106, 4160–4165.
[4] Bonemann, G., Pietrosiuk, A., Diemand, A., Zentgraf, H. and Mogk, A. (2009) Remodelling of VipA/VipB tubules by ClpV-mediated threading is crucial for type VI protein secretion. EMBO J. 28, 315–325.
[5] Basler, M., Pilhofer, M., Henderson, G.P., Jensen, G.J. and Mekalanos, J.J. (2012) Type VI secretion requires a dynamic contractile phage tail-like structure. Nature 483, 182–186.
[6] Lossi, N.S., Manoli, E., Forster, A., Dajani, R., Pape, T., Freemont, P. and Filloux, A. (2013) The HsiB1C1 (TssB-TssC) complex of the *Pseudomonas aeruginosa* type VI secretion system forms a bacteriophage tail sheathlike structure. J. Biol. Chem. 288, 7536–7548.
[7] Pukatzki, S., McAuley, S.B. and Miyata, S.T. (2009) The type VI secretion system: translocation of effectors and effector-domains. Curr. Opin. Microbiol. 12, 11–17.
[8] Russell, A.B., Hood, R.D., Bui, N.K., LeRoux, M., Vollmer, W. and Mougous, J.D. (2011) Type VI secretion delivers bacteriolytic effectors to target cells. Nature 475, 343–347.
[9] Russell, A.B., Singh, P., Brittnacher, M., Bui, N.K., Hood, R.D., Carl, M.A., Agnello, D.M., Schwarz, S., Goodlett, D.R., Vollmer, W. and Mougous, J.D. (2012) A widespread bacterial type VI secretion effector superfamily identified using a heuristic approach. Cell Host Microbe 11, 538–549.
[10] Brooks, T.M., Unterweger, D., Bachmann, V., Kostiuk, B. and Pukatzki, S. (2013) Lytic activity of the *Vibrio cholerae* type VI secretion toxin VgrG-3 is inhibited by the antitoxin TsaB. J. Biol. Chem. 288, 7618–7625.
[11] Whitney, J.C., Chou, S., Russell, A.B., Biboy, J., Gardiner, T.E., Ferrin, M.A., Brittnacher, M., Vollmer, W. and Mougous, J.D. (2013) Identification, structure, and function of a novel type VI secretion peptidoglycan glycoside hydrolase effector-immunity pair. J. Biol. Chem. 288, 26616–26624.
[12] Dong, T.G., Ho, B.T., Yoder-Himes, D.R. and Mekalanos, J.J. (2013) Identification of T6SS-dependent effector and immunity proteins by Tn-seq in *Vibrio cholerae*. Proc. Natl. Acad. Sci. USA 110, 2623–2628.
[13] Russell, A.B., LeRoux, M., Hathazi, K., Agnello, D.M., Ishikawa, T., Wiggins, P.A., Wai, S.N. and Mougous, J.D. (2013) Diverse type VI secretion phospholipases are functionally plastic antibacterial effectors. Nature 496, 508–512.
[14] Benz, J., Sendlmeier, C., Barends, T.R. and Meinhart, A. (2012) Structural insights into the effector-immunity system Tse1/Tsi1 from *Pseudomonas aeruginosa*. PLoS ONE 7, e40453.
[15] Ding, J., Wang, W., Feng, H., Zhang, Y. and Wang, D.C. (2012) Structural insights into the *Pseudomonas aeruginosa* type VI virulence effector Tse1 bacteriolysis and self-protection mechanisms. J. Biol. Chem. 287, 26911–26920.
[16] Shang, G., Liu, X., Lu, D., Zhang, J., Li, N., Zhu, C., Liu, S., Yu, Q., Zhao, Y., Zhang, H., Hu, J., Cang, H., Xu, S. and Gu, L. (2012) Structural insight into how *Pseudomonas aeruginosa* peptidoglycanhydrolase Tse1 and its immunity protein Tsi1 function. Biochem. J. 448, 201–211.
[17] Zhang, H., Gao, Z.Q., Su, X.D. and Dong, Y.H. (2012) Crystal structure of type VI effector Tse1 from Pseudomonas aeruginosa. FEBS Lett. 586, 3193–3199.
[18] Dong, C., Zhang, H., Gao, Z.Q., Wang, W.J., She, Z., Liu, G.F., Shen, Y.Q., Su, X.D. and Dong, Y.H. (2013) Structural insights into the inhibition of type VI effector Tae3 by its immunity protein Tai3. Biochem. J. 454, 59–68.
[19] Zhang, H., Zhang, H., Gao, Z.Q., Wang, W.J., Liu, G.F., Xu, J.H., Su, X.D. and Dong, Y.H. (2013) Structure of the type VI effector-immunity complex (Tae4-Tai4) provides novel insights into the inhibition mechanism of the effector by its immunity protein. J. Biol. Chem. 288, 5928–5939.
[20] Li, L., Zhang, W., Liu, Q., Gao, Y., Gao, Y., Wang, Y., Wang, D.Z., Li, Z. and Wang, T. (2013) Structural Insights on the bacteriolytic and self-protection mechanism of muramidase effector Tse3 in *Pseudomonas aeruginosa*. J. Biol. Chem. 288, 30607–30613.
[21] Wang, T., Ding, J., Zhang, Y., Wang, D.C. and Liu, W. (2013) Complex structure of type VI peptidoglycan muramidase effector and a cognate immunity protein. Acta Crystallogr. D Biol. Crystallogr. 69, 1889–1900.
[22] Silverman, J.M., Agnello, D.M., Zheng, H., Andrews, B.T., Li, M., Catalano, C.E., Gonen, T. and Mougous, J.D. (2013) Haemolysin coregulated protein is an exported receptor and chaperone of type VI secretion substrates. Mol. Cell 51, 584–593.
[23] Zhang, J., Zhang, H., Liu, Y., Zhan, L., She, Z., Dong, C. and Dong, Y. (2014) Crystallization and preliminary X-ray study of TsiV3 from *Vibrio cholerae*. Acta Crystallogr. F.
[24] Otwinowski, Z. and Minor, W. (1997) Processing of X-ray diffraction data collected in oscillation mode in: Methods in enzymology (Carter, Charles W. JrJr, Ed.), pp. 307–326, Academic Press.
[25] Terwilliger, T.C., Adams, P.D., Read, R.J., McCoy, A.J., Moriarty, N.W., Grosse-Kunstleve, R.W., Afonine, P.V., Zwart, P.H. and Hung, L.W. (2009) Decision-making in structure solution using Bayesian estimates of map quality: the PHENIX AutoSol wizard. Acta Crystallogr. D Biol. Crystallogr. 65, 582–601.
[26] McCoy, A.J., Grosse-Kunstleve, R.W., Adams, P.D., Winn, M.D., Storoni, L.C. and Read, R.J. (2007) Phaser crystallographic software. J. Appl. Crystallogr. 40, 658–674.
[27] Grosse-Kunstleve, R.W. and Adams, P.D. (2003) Substructure search procedures for macromolecular structures. Acta Crystallogr. D Biol. Crystallogr. 59, 1966–1973.
[28] Terwilliger, T.C., Grosse-Kunstleve, R.W., Afonine, P.V., Moriarty, N.W., Zwart, P.H., Hung, L.W., Read, R.J. and Adams, P.D. (2008) Iterative model building, structure refinement and density modification with the PHENIX AutoBuild wizard. Acta Crystallogr. D Biol. Crystallogr. 64, 61–69.
[29] Emsley, P. and Cowtan, K. (2004) Coot: model-building tools for molecular graphics. Acta Crystallogr. D Biol. Crystallogr. 60, 2126–2132.
[30] Afonine, P.V., Grosse-Kunstleve, R.W., Echols, N., Headd, J.J., Moriarty, N.W., Mustyakimov, M., Terwilliger, T.C., Urzhumtsev, A., Zwart, P.H. and Adams, P.D. (2012) Towards automated crystallographic structure refinement with phenix.refine. Acta Crystallogr. D Biol. Crystallogr. 68, 352–367.
[31] Chen, V.B., Arendall 3rd, W.B., Headd, J.J., Keedy, D.A., Immormino, R.M., Kapral, G.J., Murray, L.W., Richardson, J.S. and Richardson, D.C. (2010) MolProbity: all-atom structure validation for macromolecular crystallography. Acta Crystallogr. D Biol. Crystallogr. 66, 12–21.
[32] DeLano, W.L. (2002) The PyMOL molecular graphics system, DeLano Scientific, San Carlos, CA, USA.
[33] Schuck, P. (2000) Size-distribution analysis of macromolecules by sedimentation velocity ultracentrifugation and lamm equation modeling. Biophys. J . 78, 1606–1619.
[34] Konarev, P.V., Volkov, V.V., Sokolova, A.V., Koch, M.H.J. and Svergun, D.I. (2003) PRIMUS: a Windows PC-based system for small-angle scattering data analysis. J. Appl. Crystallogr. 36, 1277–1282.

[35] Svergun, D.I. (1992) Determination of the regularization parameter in indirect-transform methods using perceptual criteria. J. Appl. Crystallogr. 25, 495–503.
[36] Svergun, D., Barberato, C. and Koch, M.H.J. (1995) CRYSOL – A program to evaluate x-ray solution scattering of biological macromolecules from atomic coordinates. J. Appl. Crystallogr. 28, 768–773.
[37] Svergun, D.I., Petoukhov, M.V. and Koch, M.H.J. (2001) Determination of domain structure of proteins from X-ray solution scattering. Biophys. J . 80, 2946–2953.
[38] Volkov, V.V. and Svergun, D.I. (2003) Uniqueness of ab initio shape determination in small-angle scattering. J. Appl. Crystallogr. 36, 860–864.
[39] Holm, L. and Rosenstrom, P. (2010) Dali server: conservation mapping in 3D. Nucleic Acids Res. 38, W545–W549.
[40] Marcotte, E.M., Monzingo, A.F., Ernst, S.R., Brzezinski, R. and Robertus, J.D. (1996) X-ray structure of an anti-fungal chitosanase from streptomyces N174. Nat. Struct. Biol. 3, 155–162.
[41] Saito, J., Kita, A., Higuchi, Y., Nagata, Y., Ando, A. and Miki, K. (1999) Crystal structure of chitosanase from *Bacillus circulans* MH-K1 at 1.6-A resolution and its substrate recognition mechanism. J. Biol. Chem. 274, 30818–30825.
[42] Fukamizo, T., Amano, S., Yamaguchi, K., Yoshikawa, T., Katsumi, T., Saito, J., Suzuki, M., Miki, K., Nagata, Y. and Ando, A. (2005) Bacillus circulans MH-K1 chitosanase: amino acid residues responsible for substrate binding. J. Biochem. 138, 563–569.
[43] Patzer, S.I., Albrecht, R., Braun, V. and Zeth, K. (2012) Structural and mechanistic studies of pesticin, a bacterial homolog of phage lysozymes. J. Biol. Chem. 287, 23381–23396.
[44] Lukacik, P., Barnard, T.J., Keller, P.W., Chaturvedi, K.S., Seddiki, N., Fairman, J.W., Noinaj, N., Kirby, T.L., Henderson, J.P., Steven, A.C., Hinnebusch, B.J. and Buchanan, S.K. (2012) Structural engineering of a phage lysin that targets gram-negative pathogens. Proc. Natl. Acad. Sci. USA 109, 9857–9862.
[45] Hibbing, M.E., Fuqua, C., Parsek, M.R. and Peterson, S.B. (2010) Bacterial competition: surviving and thriving in the microbial jungle. Nat. Rev. Microbiol. 8, 15–25.